Anisotropic ^{11}B and ^{13}C NMR Interaction Tensors in Decamethylcyclopentadienyl Boron Complexes

Robert W. Schurko,*,† Ivan Hung,† Siri Schauff,† Charles L. B. Macdonald,‡ and Alan H. Cowley‡

Department of Chemistry and Biochemistry, University of Windsor, Windsor, Ontario, Canada N9B 3P4, and Department of Chemistry and Biochemistry, University of Texas at Austin, Austin, Texas 78712

Received: March 25, 2002; In Final Form: June 25, 2002

Solid-state double-resonance and triple-resonance ^{13}C, ^{11}B, and ^{1}H NMR experiments are used to investigate two main group metallocene complexes: the decamethylcyclopentadienylborinium cation, $[Cp^*_2B]^+$, and bis-(pentamethylcyclopentadienyl)methylborane, Cp^*_2BMe. The crystal structure for the latter complex is reported herein. A combination of magic-angle-spinning and static $^{11}B\{^1H\}$ NMR experiments are used to measure ^{11}B nuclear quadrupole coupling constants (C_Q) and rare instances of anisotropic boron chemical shielding tensors. Boron-11 nuclear quadrupole coupling constants reflect the higher spherical symmetry of $[Cp^*_2B]^+$ compared to Cp^*_2BMe, with $C_Q(^{11}B) = 1.14$ MHz in the former and $C_Q(^{11}B) = 4.52$ MHz in the latter. Chemical shielding tensor spans are measured for $[Cp^*_2B]^+$ and Cp^*_2BMe as $\Omega = 73.0$ and 146.0 ppm, respectively. Hartree−Fock and hybrid density functional theory (B3LYP) calculations of electric field gradient and chemical shielding tensors are in quantitative agreement with experiment, and are applied to examine the relationships between the anisotropic NMR interaction tensors and the structure and symmetry of these chemically analogous but structurally dissimilar boron complexes. Variable-temperature ^{11}B MAS NMR, ^{13}C CPMAS NMR, and $^{13}C/^{11}B/^{1}H$ CP TRAPDOR NMR experiments are applied to make a preliminary investigation of motion of the Cp* rings of $[Cp^*_2B]^+$.

Introduction

Transition metal metallocenes, such as ferrocene, have long been the focus of structure and reactivity studies in organometallic chemistry. However, more recently there have been many reports of syntheses and structural characterizations of main group metallocenes from groups 1, 2, 13, 14, and 15.[1−4] Such main group metallocenes are of great interest, not only on account of their structural diversity and the discovery of structural types that are not observed for their d-block analogues, but also because of potential industrial applications as materials precursors, polymerization catalysts, and CVD sources for ultrapure metals. Some of the main group metallocenes that feature lighter first row elements, such as the decamethylborocenium cation, $[Cp^*_2B]^+$,[5,6] and beryllocene, Cp'_2Be, represent examples of "tightly squeezed" isoelectronic metallocenes ($Cp' = C_5R_5$, R = H[7], R = Me[8]). In the former, only one of the pentamethylcyclopentadienyl rings has η^5-coordination with the boron center, while the other ring is η^1-coordinated. The $[(C_5R_5)_2B]^+$ cations (R = H, Me) have been the subject of a recent computational investigation, from which it was concluded that there may be fluxional degrees of hapticity between the two rings.[9] For example, one ring can be η^1-coordinated initially, progress through an η^2-arrangement, and end up as η^5-coordinated. Addition of a third ligand to the boron center generates a tricoordinate borane, in which both of the Cp* rings are expected to be η^1-coordinated.

From the perspective of solid-state nuclear magnetic resonance, metallocenes represent a wonderful opportunity to study the central metal quadrupolar (i.e., spin > 1/2) nuclei in a fascinating array of structurally and chemically tunable molecules. Main group metallocenes can be synthesized that possess nonbridged or bridged Cp′ rings of variable hapticity, diverse ring substituents, variable ring dynamics, and linear or bent geometries about the central nucleus depending on the steric and electronic characteristics of the substituents. Many of the main group metallocenes currently under investigation in our laboratory possess quadrupolar nuclei that are amenable to solid-state NMR analysis by virtue of their small nuclear quadrupole moments, high natural abundances, and substantial magnetogyric ratios. The manifestation of the second-order quadrupolar interaction in magic-angle-spinning (MAS) spectra of half-integer quadrupolar nuclei should provide much insight into the electronic environment and symmetry at the metal or metalloid centers of these metallocenes. Moreover, variable-temperature double- and triple-resonance solid-state NMR experiments are useful for providing enhanced understanding of ring dynamics in such systems.

The present paper is devoted to a solid-state ^{11}B and ^{13}C NMR spectroscopic analysis of the borocenium cation in the salt $[Cp^*_2B][AlCl_4]$ and the tricoordinate borane Cp^*_2BMe, the structures of which are illustrated in Figure 1. The X-ray structure of the former compound has been published elsewhere;[5] the X-ray analysis and synthesis of the latter compound is included herein. From a combination of MAS and static ^{11}B NMR experiments, the ^{11}B quadrupolar parameters (i.e., nuclear quadrupole coupling constants, C_Q, and asymmetry parameters, η_Q) and boron chemical shielding tensors in these complexes have been determined. Boron-11 is an excellent NMR nucleus for studies of this type, with nuclear spin $I = 3/2$, high natural abundance (80.42%), a relatively small nuclear quadrupole

* To whom correspondence should be addressed.
† University of Windsor.
‡ University of Texas at Austin.

10.1021/jp020800r CCC: $22.00
Published on Web 09/27/2002

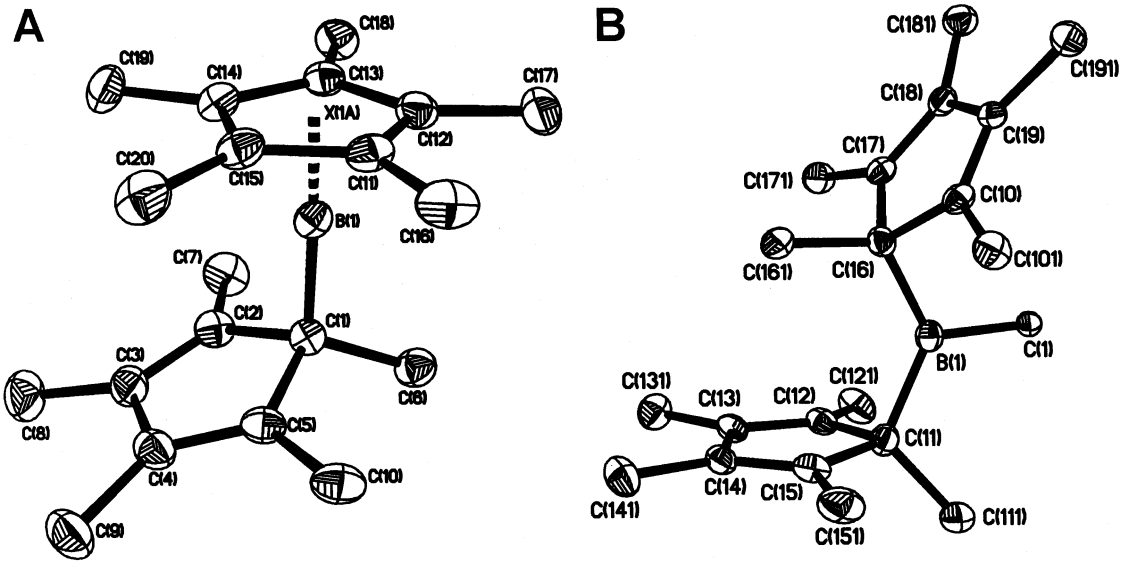

Figure 1. ORTEP drawings of the (A) $[Cp^*_2B]^+$ cation in $[Cp^*_2B][AlCl_4]$ and (B) Cp^*_2BMe.

moment = 0.04100×10^{-28} m^2,[10] and high magnetogyric ratio = 8.5847×10^7 rad T^{-1} s^{-1} (Larmor frequency of 115.589 MHz at $B_0 = 8.46$ T). There is an abundance of ^{11}B quadrupolar data in the literature for three- and four-coordinate boron complexes; however, very few definitive cases of boron chemical shielding anisotropy have been reported.[11,12] The standard boron chemical shift range is approximately 230 ppm,[13] including inorganic and organometallic boron complexes and boranes.

In addition to the foregoing, we have examined the $[Cp^*_2B]^+$ cation using variable-temperature ^{11}B MAS NMR, ^{13}C CPMAS NMR, and ^{11}B/^{13}C/^{1}H CP TRAPDOR[14] NMR experiments. The quadrupolar powder pattern, the effectiveness of cross-polarization, and efficiency of the TRAPDOR effect all indicate the existence of rapid rotation of the η^5-Cp* ring, and hitherto undescribed motions of the η^1-Cp* ring in the solid state.

Experimental Section

Synthesis of Bis(pentamethylcyclopentadienyl)methylborane, Cp^*_2BMe. A solution of MeLi in Et_2O (4.6 mL of a 1.4 M solution, 6.4 mmol) was added to a solution of $(C_5Me_5)_2BCl$ (2.03 g, 6.4 mmol) in Et_2O at −40 °C. The pale yellow mixture was stirred overnight. Volatiles were removed in vacuo, and the resulting white powder was extracted with consecutive portions of hexane and dried under vacuum. Colorless crystals were obtained by sublimation of the remaining white residue at 45 °C and 0.04 Torr. Yield: 75%. mp 57−58 °C. CI HRMS: calcd for $C_{21}H_{33}B_1$, 296.2675; found, 296.2687. NMR (C_6D_6): ^{1}H: δ 0.389 (s, B*Me*), δ 1.595 (s, C_5*Me*$_5$). ^{13}C{^{1}H}: δ 13.442 (s, C_5*Me*$_5$), δ 124.440 (s, *C*$_5$Me$_5$). ^{11}B: δ 85.625.

X-ray Crystallography of Bis(pentamethylcyclopentadienyl)methylborane, Cp^*_2BMe. The crystal used for the diffraction experiments was handled, selected, and coated in perfluoro(poly)ether prior to data collection. The data were collected on a Nonius Kappa CCD diffractometer using a graphite monochromator with Mo Kα radiation ($\lambda = 0.710\ 73$ Å). A total of 103 frames of data were collected using ω-scans with a scan range of 1° and a counting time of 20 s per frame. The data were collected at −120 °C using an Oxford Cryostream low-temperature device. Details of crystal data, data collection, and structure refinement are listed in Table 1. Data reduction was performed using DENZO-SMN.[15] The structure was solved by direct methods using SIR97[16] and refined by full-matrix least squares on F^2 with anisotropic displacement parameters for all the non-H atoms using SHELXL-93.[17] All hydrogen atoms were placed in calculated positions (AFIX 137). The function $\sum w(|F_o|^2 - |F_c|^2)^2$ was minimized, where $w = 1/[(\sigma(F_o))^2 + (0.0713P)^2 + (1.7084P)]$ and $P = (|F_o|^2 + 2|F_c|^2)/3$. No correction for secondary extinction effects was necessary. Neutral atom scattering factors and values used to calculate the linear absorption coefficient are from the International Tables for X-ray Crystallography (1992).[18] All figures were generated using SHELXTL/PC.[19] Tables of positional and thermal parameters and metrical parameters are provided in the Supporting Information.

TABLE 1: Summary of X-ray Crystallographic Data for Cp^*_2BMe

empirical formula	$C_{21}H_{33}B$
formula weight	296.28
temperature (K)	153(2)
wavelength (Å)	0.710 73
crystal system	orthorhombic
space group	$P2_12_12_1$
unit cell dimensions	
a (Å)	7.5688 (15)
b (Å)	17.863 (4)
c (Å)	27.857 (6)
α (deg)	90
β (deg)	90
γ (deg)	90
volume (Å^3)	3766.4 (13)
Z	8
calculated density (g cm^{-3})	1.045
absorption coefficient (mm^{-1})	0.057
F(000)	1312
crystal size (mm)	0.4 × 0.4 × 0.2
θ range for data collection (deg)	2.92−27.48
limiting indices	$-9 \le h \le 9$
	$-23 \le k \le 23$
	$-36 \le l \le 35$
reflections collected/unique	7702/7702 [$R_{(int)} = 0.0600$]
refinement method	full-matrix least squares on F^2
data/restraints/parameters	7702/0/419
goodness-of-fit on F^2	1.017
final R indices [$I > 2\sigma(I)$]	R1 = 0.0696, wR2 = 0.1416
R indices (all data)	R1 = 0.1413, wR2 = 0.1783
largest diff peak and hole (e Å^{-3})	0.189 and −0.255

Solid-State NMR. Samples were prepared under an N_2 environment and packed into 3.2 mm o.d. rotors. Spectra were acquired on an 8.46 T (υ_0(^{1}H) = 360 MHz) Chemagnetics CMX-360 NMR spectrometer at the State University of New

York at Stony Brook (courtesy of Prof. Clare P. Grey), with $\upsilon_0(^{11}B) = 115.515$ MHz and $\upsilon_0(^{13}C) = 90.536$ MHz. A Chemagnetics 3.2 mm triple-resonance HXY probe was applied for all experiments. For ^{11}B NMR experiments, solid $NaBH_4$ was used as a secondary chemical shift reference, with $\delta_{iso}(^{11}B) = -42.06$ ppm, setting the chemical shift scale against the primary reference, which is neat liquid $(C_2H_5)_2O{\cdot}BF_3$ with $\delta_{iso}(^{11}B) = 0.00$ ppm.[20] ^{13}C NMR spectra were referenced to TMS ($\delta_{iso}(^{13}C) = 0.0$ ppm) by setting the high-frequency resonance of adamantane to 38.57 ppm. Proton-decoupled ^{11}B MAS NMR spectra were acquired with spinning speeds ranging from 5 to 20 kHz, with pulse widths of 1.5 μs, $\upsilon_1 = 80$ kHz, and recycle delays of 1 s. Proton-decoupled ^{11}B Hahn echo experiments were conducted with similar pulse widths and recycle delays, with interpulse delays of 50−100 μs. Proton-decoupled ^{13}C MAS, CPMAS, and VACPMAS NMR spectra were acquired at spinning speeds of 2−6 kHz with proton 90° pulse widths of 2.5 μs, recycle delays from 2 to 8 s, and contact times ranging from 0.1 to 15 ms. Rotor-synchronized $^{13}C/^{1}H/^{11}B$ CPMAS TRAPDOR experiments were conducted in a manner similar to the ^{13}C CPMAS experiments above, except with strong on-resonance irradiation of the ^{11}B peaks with a rf field of 80 kHz over one, three, and five rotor cycle periods.

Spectral Simulations. Analytical simulations of the ^{11}B MAS and static NMR spectra were carried out on a Pentium III computer using the WSOLIDS simulation package.[21] This software incorporates the space-tiling method of Alderman and co-workers for the generation of frequency domain solid-state NMR powder patterns.[22] Carbon shielding tensors were extracted from ^{13}C MAS NMR spectra using the method of Herzfeld and Berger.[23] Prior to simulating ^{11}B MAS NMR spectra, the sidebands were summed into the isotropic centerband to produce a powder pattern resembling that obtained at infinite spinning speeds.

Numerical simulations of the full central transition spinning sideband manifold were performed using the SIMPSON[24] software package for general simulations of solid-state NMR spectra. Simulations were accomplished by the *gcompute* method of powder averaging using the *zcw4180* crystal file provided in the package. For the sake of simplicity, the start and detect operators were set to I_{1x} and I_{1p}, respectively, requiring us only to set the delay parameter to 9999 μs in the pulse sequence section. Simulated spectra were saved in free induction decay (FID) format as ASCII files without any mathematical manipulation and converted for processing to NUTS (Acorn NMR) readable files using a script written within our research group.

Ab Initio Calculations. Calculations of electric field gradient and chemical shielding tensors were performed using the Gaussian 98[25] computational package on a Dell Precision 420 workstation with dual 733 MHz Pentium III processors running Red Hat Linux 6.2 (Zoot). Molecular coordinates of $[Cp^*_2B]^+$ and Cp^*_2BMe used in calculations were obtained from crystal structure data resolved by X-ray diffraction studies from ref 5 and the present work, respectively. Computations were carried out using the restricted Hartree−Fock (RHF) method and density functional theory (DFT) with the B3LYP functional[26,27] in conjunction with basis sets (6-31G**, 6-311G**, 6-311+G**) provided by the Gaussian 98 package. Chemical shielding tensors were calculated using the GIAO method.[28] Due to the lack of a standard ^{11}B absolute chemical shielding scale, calculated chemical shielding data were referenced to theoretical BH_4^- isotropic chemical shielding as a secondary reference using $\delta_{iso}(BH_4^-) = -42.06$ ppm, which sets the chemical shift scale to that of $(C_2H_5)_2O{\cdot}BF_3$ ($\delta_{iso} = 0.0$ ppm). This was carried out by subtracting theoretical chemical shielding data of $[Cp^*_2B]^+$ and Cp^*_2BMe from those of BH_4^-, which were calculated using the corresponding methods and basis sets, and then adding −42.06 ppm. Carbon chemical shielding parameters were converted to carbon chemical shifts by calculating the absolute chemical shielding of the carbon nucleus in C≡O, and setting the chemical shift to the experimentally determined value of $\delta_{iso}(^{13}C) = 187.1$ ppm with respect to the carbon nucleus in TMS ($\delta_{iso}(^{13}C) = 0.0$ ppm).[29] The rotational barrier of the η^5-Cp* ring in $[Cp^*_2B]^+$ was determined by calculating the self-consistent-field (SCF) energy of the molecule, keeping all atoms fixed and rotating the η^5-Cp* ring by six degree intervals. Movement of the η^5-Cp* ring was accomplished using the *z*-matrix input format. Calculations were also conducted in which the entire molecular geometry was allowed to optimize except for the angle responsible for the relative orientation of the Cp* rings.

Results and Discussion

In this section we discuss the experimental and theoretical measurement of two NMR interaction tensors: the electric field gradient (EFG) tensor, $\bar{\mathbf{V}}$, and the chemical shielding (CS) tensor, $\bar{\boldsymbol{\sigma}}$. Both $\bar{\mathbf{V}}$ and $\bar{\boldsymbol{\sigma}}$ are second-rank tensors with nine components: $\bar{\boldsymbol{\sigma}} = \{\sigma_{\alpha\beta};\ \alpha, \beta = x, y, z\}$ and $\bar{\mathbf{V}} = \{V_{\alpha\beta};\ \alpha, \beta = x, y, z\}$. The origins of NMR powder patterns affected by these anisotropic NMR interaction tensors are well discussed elsewhere.[30,31] The EFG tensor, $\bar{\mathbf{V}}$, is traceless and symmetric, and can be expressed in its own principal axis system (PAS) by three principal components assigned such that $|V_{11}| \leq |V_{22}| \leq |V_{33}|$. This can be further reduced to two commonly reported parameters: the nuclear quadrupole coupling constant, $C_Q = eQV_{33}/h$ (in MHz), and the quadrupolar asymmetry parameter $\eta_Q = (V_{11} - V_{22})/V_{33}$, where $0 \leq \eta_Q \leq 1$. The chemical shielding tensor, $\bar{\boldsymbol{\sigma}}$, has a nonzero trace and is asymmetric, though the asymmetric components of the CS tensor do not make an observable contribution to the NMR spectrum. The CS tensor describes the shielding of a nucleus relative to the bare nucleus, which has chemical shielding of 0 ppm (i.e., no shielding), and has three principal components in its PAS which are assigned from least to most shielded as $\sigma_{11} \leq \sigma_{22} \leq \sigma_{33}$. Under conditions of rapid random tumbling, only the isotropic chemical shielding is observed, and is given by $\sigma_{iso} = (\sigma_{11} + \sigma_{22} + \sigma_{33})/3$. Chemical shielding is often described with respect to a reference compound (i.e., the chemical shift), which typically has sharp resonance(s) that is (are) arbitrarily assigned some chemical shift value. The chemical shift tensors also has three components which are assigned from least to most shielded as $\delta_{11} \geq \delta_{22} \geq \delta_{33}$, with $\delta_{iso} = (\delta_{11} + \delta_{22} + \delta_{33})/3$. Chemical shift and chemical shielding are related to one another via $\delta_{sample} = (\sigma_{ref} - \sigma_{sample})/(1 - \sigma_{ref}) \times 10^6 \approx \sigma_{ref} - \sigma_{sample}$. Two additional parameters, the span and the skew, are derived from the three principal components. The span of the CS tensor, Ω, is used to describe the range of chemical shielding anisotropy, with $\Omega = \sigma_{33} - \sigma_{11} = \delta_{11} - \delta_{33}$. The skew, κ, describes the degree of axial symmetry of the CS tensor, with $\kappa = 3(\sigma_{iso} - \sigma_{22})/\Omega = 3(\delta_{22} - \delta_{iso})/\Omega$, where $-1 \leq \kappa \leq +1$.[32]

In performing time-independent analytical simulations of MAS NMR spectra of quadrupolar nuclei, we neglect the effects of chemical shielding anisotropy by assuming infinite spinning speed conditions. The appearance of the MAS NMR spectrum is therefore dependent upon only three parameters: C_Q, η_Q, and δ_{iso}. In the case of static NMR spectra (i.e., stationary sample), the anisotropic chemical shielding is not averaged, and the Ω and κ make contributions to the appearance of the spectrum. In

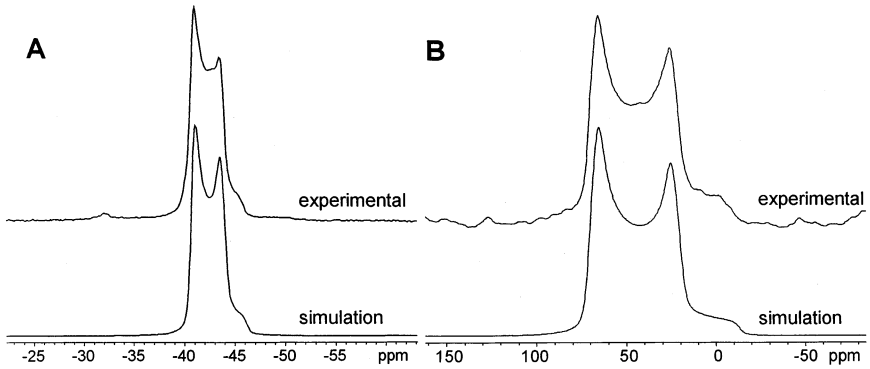

Figure 2. Experimental and simulated $^{11}B\{^1H\}$ MAS NMR spectra at 8.46 T of (A) $[Cp^*_2B][AlCl_4]$, $\upsilon_{rot} = 6.0$ kHz, and (B) Cp^*_2BMe, $\upsilon_{rot} = 20.0$ kHz.

TABLE 2: Experimental Boron-11 Chemical Shift and Quadrupolar Parameters in $[Cp^*_2B][AlCl_4]$ and Cp^*_2BMe

parameter	$[Cp^*_2B][AlCl_4]$	Cp^*_2BMe
C_Q (MHz)	1.14 (1)	4.52 (2)
η_Q[a]	0.10 (4)	0.11 (1)
δ_{iso} (ppm)	−41.3 (1)	81.9 (1)
Ω[b] (ppm)	73.0 (3)	146.1 (3)
κ[c]	0.98 (2)	0.75 (4)
δ_{11}[d] (ppm)	−16.7	136.7
δ_{22} (ppm)	−17.5	118.4
δ_{33} (ppm)	−89.7	−9.4

[a] Quadrupolar asymmetry parameter, $\eta_Q = (V_{11} - V_{22})/V_{33}$. [b] Span of the CS tensor, $\Omega = \delta_{11} - \delta_{33}$. [c] Skew of the CS tensor, $\kappa = 3(\delta_{22} - \delta_{iso})/\Omega$. [d] Principal components of the CS tensor from least to most shielded: $\delta_{11} \geq \delta_{22} \geq \delta_{33}$.

addition, the relative orientation of the CS and EFG tensors plays a role in determining the shape of the static powder pattern.[33,34] The relative orientations of these tensors are described by Euler angles α, β, and γ,[35] where the CS tensor is described in the EFG PAS by the rotational operation $R(\alpha,\beta,\gamma) = R_{Z''}(\gamma)\, R_{Y'}(\beta)\, R_Z(\alpha)$, where α and γ range from 0 to 2π and β ranges from 0 to π. Complete fitting of a static NMR spectrum involves a simulation dependent upon eight independent variables, though the problem can be reduced to five variables by using data obtained from concomitant MAS NMR spectra. Numerical time-dependent simulations are used (see Experimental Section for details) to examine the combined effects of the quadrupolar interaction, the chemical shielding anisotropy, and magic-angle spinning in solid-state NMR spectra. Such simulations rely on the numerical evaluation of the time-dependent Liouville−von Neumann equation of motion, with high-field truncated Hamiltonians describing the quadrupolar and chemical shielding interactions in the Zeeman frame.[30,31]

Boron-11 MAS NMR. Boron-11 MAS NMR spectra of $[Cp^*_2B]^+$ and Cp^*_2BMe and best fit simulations are shown in parts A and B, respectively, of Figure 2. The parameters from these simulations (Table 2) are obtained from comparison of simulations of complementary MAS and static (vide infra) NMR spectra. As the local environment of the boron changes from the "two-coordinate" η^1,η^5-arrangement in $[Cp^*_2B]^+$ to the three-coordinate η^1,η^1,Me-arrangement in Cp^*_2BMe, there are two conspicuous differences apparent in the NMR parameters: (i) a substantial increase in the ^{11}B nuclear quadrupole coupling constant, $C_Q(^{11}B)$, and (ii) considerable deshielding of the boron nucleus. The $C_Q(^{11}B)$ increases from 1.14 MHz in $[Cp^*_2B]^+$ to 4.52 MHz in Cp^*_2BMe, whereas the asymmetry parameters, η_Q, remain similar. A small distortion is visible in the ^{11}B MAS NMR spectra of $[Cp^*_2B]^+$, which is identified as arising from impurities in the accompanying static spectra (vide infra). The latter $C_Q(^{11}B)$ is comparable to that measured in trimesitylborane ($C_Q(^{11}B) = 4.75$ MHz),[11] with which it is structurally similar.

It has been demonstrated that certain special arrangements of point charges about the vertices of centrosymmetric polyhedra can generate a zero EFG tensor at the center of the polyhedra, S_0.[36,37] This simple model can be used to rationalize the differences in nuclear quadrupolar coupling constants in these compounds. In the case of $[Cp^*_2B]^+$, we can imagine the boron nucleus at the center of an icosahedron (i.e., 12 vertices, 20 faces), with the nearest-neighbor carbons (i.e., five from the η^5-Cp* ring and one from the η^1-Cp* ring) approximately positioned on six of the twelve vertices. In general, the null EFG occurs at the center of a centrosymmetric polyhedron with V vertexes if like point charges are placed at $V/2$ of the vertices such that none of them are related by reflection through the center point, S_0.[37] However, this is of course not exactly the case for this molecule, since (i) the η^5-Cp* ring carbons are not positioned *precisely* on the icosahedron vertices, and possess different charges than the η^1-coordinated Cp* ring carbon, and (ii) the EFG at the boron is sensitive to the presence of second-coordination sphere atoms, such as methyl carbons, noncoordinated η^1-ring carbons, protons, etc. Nonetheless, this spherical pseudosymmetry likely accounts for the smaller value of $C_Q(^{11}B)$ in $[Cp^*_2B]^+$ compared to that measured in Cp^*_2BMe. In the case of Cp^*_2BMe, the BC_3 skeletal geometry is trigonal planar; however, overall the molecular symmetry is C_1 and consequently the observed value of $C_Q(^{11}B)$ is very large.

Of equal interest is the difference in nuclear shielding in the ^{11}B NMR spectra of these two complexes. The boron chemical shift range is typically quoted as being ca. +20 to −130 ppm for four-coordinate boron compounds and ca. +100 to −10 ppm for three-coordinate boron.[13] The three-coordinate Cp^*_2BMe has a boron chemical shift of 81.9 ppm, which is comparable to the high chemical shift values of most three-coordinate organometallic boron complexes. In $[Cp^*_2B]^+$, the presence of one η^5-Cp* ring and one η^1-Cp* ring results in a large increase in nuclear shielding, with $\delta_{iso}(^{11}B) = -41.3$ ppm. Such a change in shielding in the presence of the η^5-Cp* ring is not surprising, as a rough perusal of solution NMR literature quickly shows that the majority of η^5-bis(cyclopentadienyl) coordinated main group metals have isotropic chemical shifts occurring to low frequency of standard chemical shift ranges. For instance, the magnesium chemical shifts normally range from 0 to 100 ppm (from reference compound $MgSO_4 \cdot 7H_2O$ to Et_2Mg);[13] however, Cp_2Mg has a chemical shift of −85.4 ppm. Substitution of various Lewis bases at the Mg site, which cause bending of the metallocene structure, result in decreased nuclear shielding (i.e., higher chemical shifts).[38] Similar results have been observed for main group metallocenes such as the aluminocenium cation,

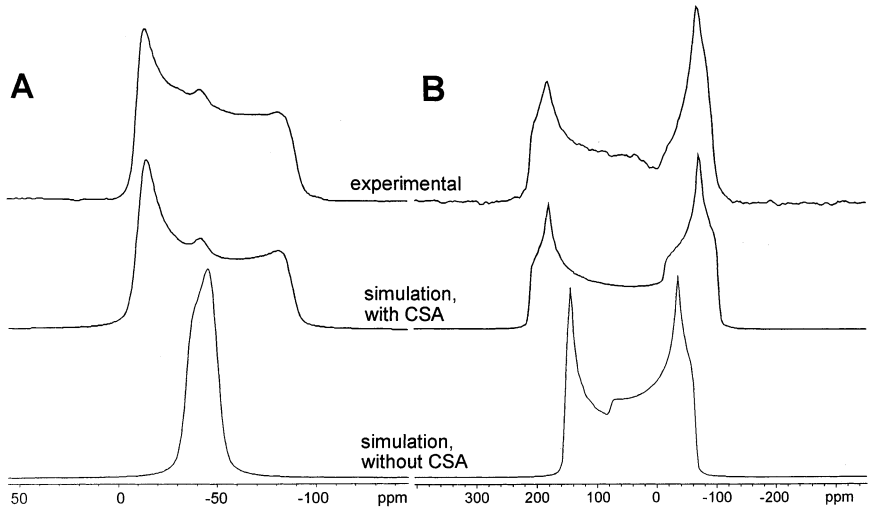

Figure 3. Experimental and simulated $^{11}B\{^1H\}$ static NMR spectra at 8.46 T of (A) $[Cp^*_2B][AlCl_4]$ and (B) Cp^*_2BMe. Simulations with and without the effects of boron chemical shielding anisotropy are included for comparison.

$\delta_{iso}(^{27}Al) = -114.5$ ppm[39] (standard shift range 0−300 ppm from $Al(H_2O)_6^{3+}$), stannocene, $\delta_{iso}(^{119}Sn) = -2199$ ppm[40] (organometallic tin complexes from −400 to 200 ppm, with respect to $SnMe_4$ at 0 ppm), and plumbocene, $\delta_{iso}(^{207}Pb) = -6150$ ppm[40] (organometallic lead complexes from −400 to +400 ppm with respect to $PbMe_4$ at 0.0 ppm). A metal with a single η^5-coordinated Cp′ ring should have a chemical shift somewhere between the limits of three-coordinate planar and bis-η^5-Cp′ coordinated metallocenes.

Boron-11 Static NMR. To better understand the origins of nuclear magnetic shielding in these complexes, static ^{11}B NMR spectra were acquired for both complexes, with a view to observing boron chemical shielding anisotropy. Simulation of the static spectrum using only the quadrupolar parameters obtained from the ^{11}B MAS NMR spectra indicate that additional anisotropic NMR interactions are present. It is clear that there is an anisotropic boron chemical shielding tensor in $[Cp^*_2B]^+$, with the following parameters obtained from best fit simulations: $\delta_{iso} = -41.3$ (1) ppm, $\Omega = 73.0$ (3) ppm, and $\kappa = 0.98(2)$ (Figure 3A). The relative orientation of the EFG and CS tensors is described by Euler angles $\alpha = \beta = \gamma = 0°$, which indicates that the largest component of the EFG tensor, V_{33}, and the most shielded component of the CS tensor, δ_{33}, are coincident. A small "hump" in the spectrum is visible at approximately −40 ppm, which results from an impurity with a relatively sharp resonance, and constitutes <1% of the total integrated signal (included in the simulated spectra).

Static ^{11}B NMR spectra and simulations for Cp^*_2BMe are pictured in Figure 3B. A larger boron chemical shielding anisotropy is present, with $\delta_{iso} = 81.9(1)$ ppm, $\Omega = 146.1(3)$ ppm, and $\kappa = 0.75(4)$. Best fit simulations indicate that the EFG and CS tensors are essentially coincident, with $\alpha = \beta = \gamma = 0°$. The range of chemical shielding anisotropy, described by the span, is comparable to that previously reported for trimesitylborane ($\Omega = 121$ (1) ppm),[11] and represents the largest boron CSA measured by solid-state NMR to date. The origin of the anisotropic boron shielding in these molecules is further investigated using ab initio methods discussed in the next section of this paper.

Experimental and best fit numerical simulations of ^{11}B MAS NMR spectra of the $[Cp^*_2B]^+$ cation ($\upsilon_{rot} = 6000$ Hz) are shown in Figure 4A and for Cp^*_2BMe in Figure 4B ($\upsilon_{rot} = 20\,000$ Hz). Numerically simulated MAS spectra using the quadrupolar and chemical shielding parameters from time-independent analytical simulations are in good agreement with experimental data. The presence of chemical shielding anisotropy at the boron center in $[Cp^*_2B]^+$ can easily be confirmed by the dramatic disappearance of spinning sidebands upon neglect of anisotropic shielding contributions to the powder pattern. A small satellite peak arising from the $\pm 3/2 \leftrightarrow \pm 1/2$ satellite transitions is observed slightly to the left of the isotropic centerband of the central transition MAS spectrum. The spinning sidebands in the ^{11}B MAS NMR spectrum of Cp^*_2BMe do not disappear completely, but are much reduced in intensity in the absence of boron chemical shielding anisotropy.

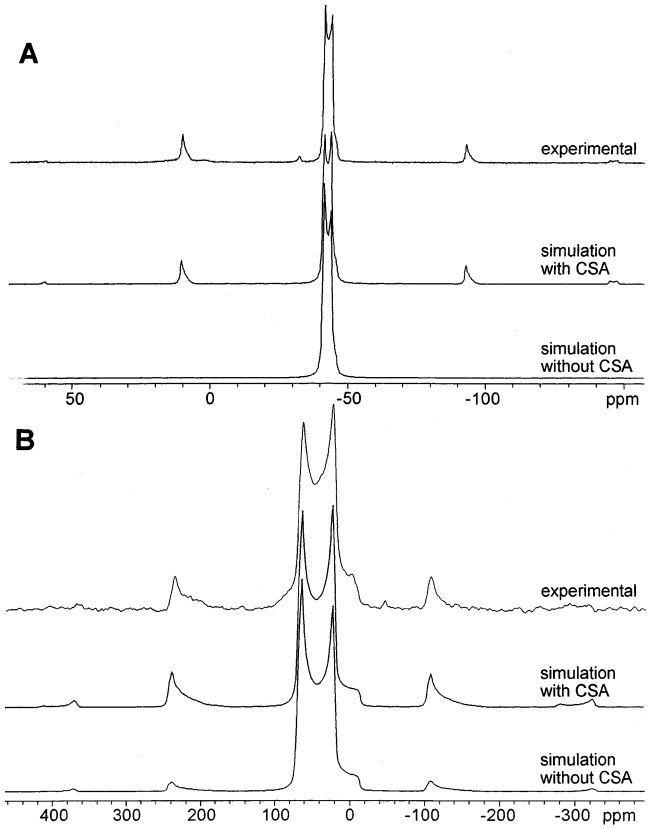

Figure 4. Experimental and numerical simulations (using Simpson) of ^{11}B MAS NMR spectra of (A) $[Cp^*_2B][AlCl_4]$ and (B) Cp^*_2BMe.

Ab Initio Calculations of Boron NMR Interaction Tensors. Introduction. Ab initio calculations of NMR parameters

represent some of the more demanding computations of molecular properties. In particular, calculations of chemical shielding tensors and indirect spin−spin coupling constants present formidable challenges to theoreticians.[41,42] Nuclear magnetic shielding is dependent upon local electronic structure about the nucleus, and under the Ramsey formalism has its origin in a diamagnetic ground-state contribution and paramagnetic contribution arising from magnetic dipole allowed mixing of occupied and virtual orbitals. There are now many instances in which ab initio calculations yield chemical shielding tensors which quantitatively match tensors obtained from solid-state powder and single-crystal NMR data.[41] Boron chemical shielding calculations with suitable basis sets on the isolated molecule should closely predict experimental results,[11,43] providing that there are no unusual molecular motions which serve to average the components of the nuclear magnetic shielding tensor which are observed experimentally.

The electric field gradient tensor is a ground-state property of the molecule, and it is very dependent upon the asymmetry of electronic charge density near the nucleus. In the past, calculations of the EFG tensor involved the use of a simple point charge model, where atoms surrounding the probe nucleus were assigned arbitrary charges, which were then summed to calculate the EFG tensor. Such point charge calculations rarely correspond closely with experimental data, as they do not account for polarization of electron density (notably the core electrons), and rely on empirically assigned charges.

Two main methods presently used for calculation of EFG tensors are ab initio and density functional theory calculations of small clusters of atoms and linear-augmented-plane-wave (LAPW) band structure calculations.[44] In the case of ordered two- and three-dimensional solids with ionic components, the latter method is thought to be superior, notably for heavier atoms where Gaussian-based orbital methods do not describe the electron density near the nucleus adequately. However, Hartree−Fock and DFT methods have been applied on isolated molecules and larger clusters of atoms in many instances to successfully calculate nuclear quadrupole coupling constants and asymmetry parameters that closely match experimental solid-state data. In solids, the EFG tensor at a nucleus is mainly dependent upon the local chemical environment, though it can be influenced by long-range electrostatic interactions with distant electric monopoles, dipoles, and quadrupoles.[45] In addition, solid-state quadrupole coupling constants are affected by changes in temperature (typically the C_Q is observed to increase with decreasing temperature), due to motions of molecules or ions within the crystalline lattice.[45] Embedded cluster molecular orbital (ECMO) calculations, which involve RHF or DFT calculations on a cluster embedded within a lattice of point charges,[46] or full-crystal DFT on periodic ionic systems,[46c,47] are often used to improve the accuracy of theoretical calculations of EFG tensors by taking into account electrostatic interactions arising from sources distant from the nucleus. In this study, only Hartree−Fock and hybrid-DFT calculations are applied to study the boron EFG tensors in the isolated molecules, as the solid is not highly ionic in nature and long-distance electrostatic interactions are not expected to significantly alter the EFG tensor at the boron nucleus. Similar calculations on boron EFGs in small molecules have previously been conducted with a high degree of success.[11,48]

Boron Electric Field Gradient Tensors. Calculations of the EFG tensors for an isolated $[Cp^*_2B]^+$ cation and an isolated Cp^*_2BMe molecule are summarized and compared with experimental data in Table 3. The values of $C_Q(^{11}B)$ are overestimated by both methods, but EFG tensors with almost axial symmetry ($\eta_Q = 0.03-0.11$) are predicted for both molecules, in close agreement with experimental results. The B3LYP calculations are closer to the experimental results than RHF calculations, and as the basis set size is increased, the $C_Q(^{11}B)$ moves further away from the experimental value. The discrepancy between experimentally determined and theoretically calculated quadrupolar parameters likely arise from the fact that intramolecular motions are not taken into account, although it is possible that there are some contributions to the EFG tensor from distant point charges in the solid lattice. The overestimation of the $C_Q(^{11}B)$ is therefore not surprising, as rapid molecular motion is most often observed to significantly decrease the magnitude of nuclear quadrupole coupling constants due to averaging of atomic positions within the molecule or ionic solid.[45] Calculations predict that the $C_Q(^{11}B)$ in Cp^*_2BMe is ca. 3.9 MHz larger than that in $[Cp^*_2B]^+$, in reasonable agreement with experimental results (3.38 MHz difference). The EFG tensor orientations in $[Cp^*_2B]^+$ and Cp^*_2BMe are pictured in Figure 5A. In $[Cp^*_2B]^+$, the largest component of the EFG tensor (V_{33}) is coincident with the η^5-Cp* ring's pseudo-5-fold axis of symmetry, while in Cp^*_2BMe it is aligned with a 3-fold axis perpendicular to the plane of the coordinated ligands. The EFG tensor is observed to be nearly axial symmetric by both experimental and theoretical methods for both $[Cp^*_2B]^+$ and Cp^*_2BMe, meaning that V_{11} and V_{22} are similar in magnitude and positioned perpendicular to the 5-fold and 3-fold axes in $[Cp^*_2B]^+$ and Cp^*_2BMe, respectively.

TABLE 3: Experimental and Theoretical Boron Quadrupolar Parameters in $[Cp^*_2B]^+$ and Cp^*_2BMe

source	V_{11}[a] (au)	V_{22} (au)	V_{33} (au)	$\lvert C_Q\rvert$[b] (MHz)	η_Q[c]
			$[Cp^*_2B]^+$		
experimental				1.14 (1)	0.10 (4)
RHF					
6-31G**	−0.072	−0.0794	0.1514	1.46	0.05
6-311G**	−0.0752	−0.0826	0.1578	1.52	0.05
6-311+G**	−0.0749	−0.0826	0.1575	1.52	0.05
DFT(B3LYP)					
6-31G**	−0.0622	−0.0665	0.1287	1.24	0.03
6-311G**	−0.0664	−0.0714	0.1378	1.33	0.04
6-311+G**	−0.066	−0.071	0.137	1.32	0.04
			Cp^*_2BMe		
experimental				4.52 (2)	0.11 (1)
RHF					
6-31G**	0.2502	0.2896	−0.5399	5.2	0.07
6-311G**	0.259	0.3035	−0.5625	5.42	0.08
6-311+G**	0.259	0.3038	−0.5628	5.42	0.08
DFT(B3LYP)					
6-31G**	0.2235	0.2671	−0.4906	4.73	0.09
6-311G**	0.2403	0.2974	−0.5377	5.18	0.11
6-311+G**	0.24	0.2974	−0.5374	5.18	0.11

[a] V_{ii} are principal components of the EFG tensor, where $|V_{33}| \geq |V_{22}| \geq |V_{11}|$. [b] The largest component of the EFG tensor, V_{33}, is converted from atomic units to C_Q in MHz by multiplying by 9.7177×10^{21} V $m^{-2} \times eQ/h$. [c] Quadrupolar asymmetry parameter, $\eta_Q = (V_{11} - V_{22})/V_{33}$.

Boron Chemical Shielding Tensors. There is remarkably good agreement between experimental boron chemical shielding tensors and those calculated by both RHF and B3LYP methods (Table 4). All chemical shielding tensor values have been converted to the boron chemical shift scale (as described in the Experimental Section) for ease of comparison with experimental results. For $[Cp^*_2B]^+$, δ_{iso} and Ω are predicted satisfactorily, and the experimental and theoretical skews match almost identically. RHF calculations overestimate the nuclear magnetic shielding in the directions of δ_{11} and δ_{33}, and B3LYP calcula-

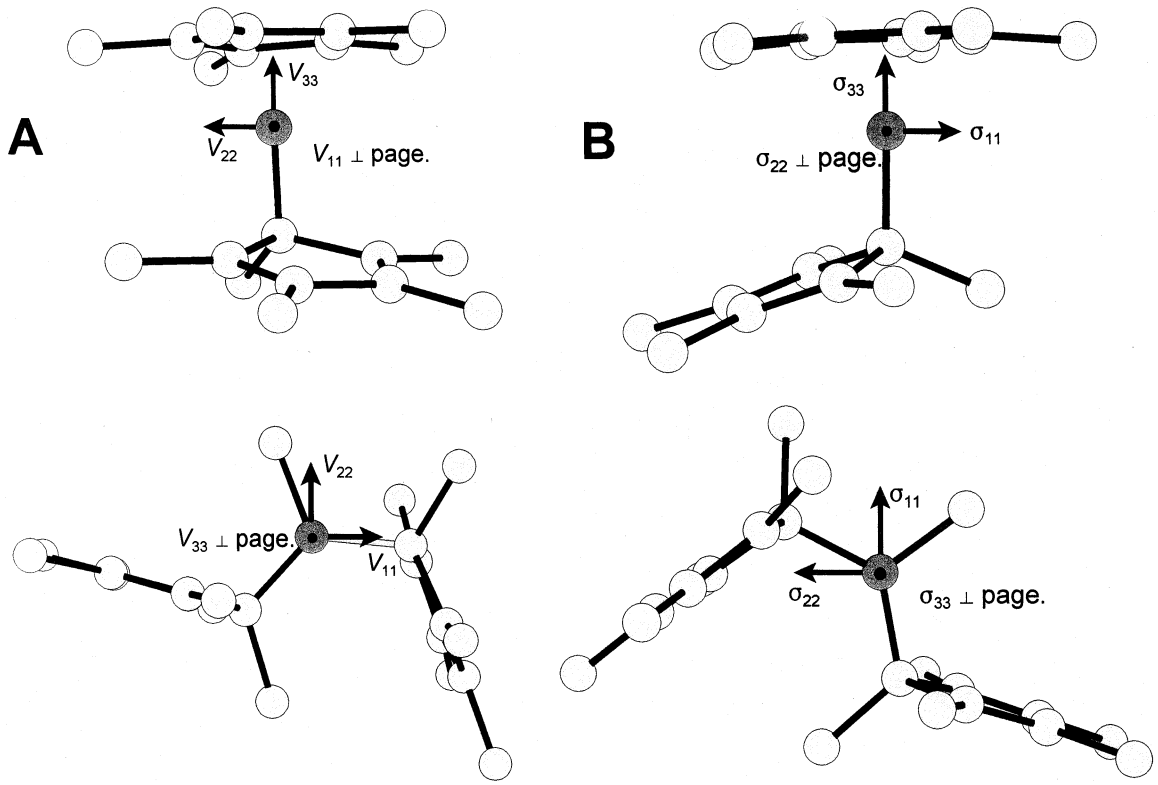

Figure 5. Theoretical (A) EFG tensor and (B) CS tensor orientations in $[Cp^*_2B]^+$ and Cp^*_2BMe.

TABLE 4: Experimental and Theoretical Boron Chemical Shift Tensors in $[Cp^*_2B]^+$ and Cp^*_2BMe[a]

source	δ_{11} (ppm)	δ_{22} (ppm)	δ_{33} (ppm)	δ_{iso} (ppm)	Ω[b] (ppm)	κ[c]
			$[Cp^*_2B]^+$			
experimental[d]	−16.7	−17.5	−89.7	−41.3 (1)	73.0 (3)	0.98 (2)
RHF						
6-31G**	−22.0	−24.8	−101.9	−49.6	79.9	0.93
6-311G**	−22.1	−24.4	−103.4	−50.0	81.3	0.94
6-311+G**	−20.5	−23.1	−102.0	−48.5	81.4	0.94
B3LYP						
6-31G**	−10.5	−14.5	−89.8	−38.3	79.3	0.90
6-311G**	−10.7	−14.0	−93.0	−39.2	82.3	0.92
6-311+G**	−8.6	−11.5	−89.7	−36.6	81.1	0.93
			Cp^*_2BMe			
experimental[d]	136.7	118.4	−17.3	81.9 (1)	146.0 (3)	0.75 (4)
RHF						
6-31G**	130.9	100.0	−12.7	72.8	143.6	0.57
6-311G**	140.4	107.9	−10.6	79.3	151.0	0.57
6-311+G**	141.8	109.5	−9.3	80.7	151.1	0.57
B3LYP						
6-31G**	143.8	108.9	−5.2	82.5	149.0	0.53
6-311G**	161.6	122.6	−2.3	93.9	163.9	0.53
6-311+G**	164.9	124.4	−0.1	96.4	164.9	0.51

[a] Geometry of $[Cp^*_2B]^+$ and Cp^*_2BMe are taken from experimental X-ray crystal structures (see Experimental Section for details). [b] Span of the CS tensor, $\Omega = \delta_{11} - \delta_{33}$. [c] Skew of the CS tensor, $\kappa = 3(\delta_{22} - \delta_{iso})/\Omega$. [d] Experimental and theoretical chemical shifts were referenced with respect to BH_4^-, $\delta(^{11}B) = -42.06$ ppm.

tions underestimate the nuclear shielding along δ_{11}. In the case of Cp^*_2BMe, RHF calculations seem slightly better than B3LYP methods in predicting experimental values. Notably, there is excellent agreement between experimental and RHF boron isotropic shifts and spans.

The orientations of the boron chemical shielding tensors in $[Cp^*_2B]^+$ and Cp^*_2BMe are pictured in Figure 5B. In $[Cp^*_2B]^+$, the most shielded component, σ_{33}, is directed approximately from the boron nucleus to the center of the η^5-Cp* ring, with σ_{11} pointing along the direction of the *ipso*-methyl carbon which "bends" away from the boron atom. The near-axial symmetry of the boron chemical shielding tensor is easily justified, when one considers the relatively homogeneous electronic environment perpendicular to the η^5-Cp*-boron bond axis. The most shielded principal component in Cp^*_2BMe is directed from the boron nucleus perpendicular to a plane containing the three directly bound carbons, while σ_{11} approximately bisects the angle between the methyl carbon and one of the boron-bound Cp* ring carbons. In this case, σ_{11} and σ_{22} point into electronically distinct environments due to the different orientations of the η^1-Cp* rings, thereby resulting in a nonaxially symmetric chemical shielding tensor; however, $\kappa = 0.75$, indicating that these two components are relatively similar to one another, and σ_{33} is the distinct principal component.

TABLE 5: Theoretical Diamagnetic and Paramagnetic Contributions to Shielding at the Boron in $[Cp^*_2B]^+$, Cp^*_2BMe, and BH_4^-

	σ_{11}^d	σ_{11}^p	σ_{22}^d	σ_{22}^p	σ_{33}^d	σ_{33}^p	σ_{iso}^d	σ_{iso}^p	σ_{iso}^{total}
				$[Cp^*_2B]^+$					
RHF/6-31G**	196.70	−57.38	199.61	−57.49	219.07	0.10	205.12	−38.25	166.87
RHF/6-311G**	191.29	−54.48	193.97	−54.86	220.30	−2.16	201.85	−37.17	164.69
RHF/6-311+G**	68.26	68.20	112.12	26.84	121.01	96.86	100.46	63.97	164.43
B3LYP/6-31G**	201.94	−77.22	203.27	−74.59	224.37	−20.32	209.86	−57.37	152.49
B3LYP/6-311G**	195.34	−74.31	196.87	−72.50	222.91	−19.61	205.04	−55.47	149.57
B3LYP/6-311+G**	70.67	50.98	108.83	15.69	122.36	80.34	100.62	49.00	149.62
				Cp^*_2BMe					
RHF/6-31G**	171.39	−185.01	201.18	−183.85	208.85	−78.87	193.81	−149.24	44.56
RHF/6-311G**	170.13	−195.86	197.04	−190.25	209.20	−83.93	192.12	−156.68	35.44
RHF/6-311+G**	150.28	−176.15	178.06	−171.64	180.43	−55.21	169.59	−134.34	35.26
B3LYP/6-31G**	180.19	−209.80	211.42	−206.08	213.69	−94.26	201.77	−170.05	31.72
B3LYP/6-311G**	174.45	−225.69	204.77	−217.08	212.34	−99.67	197.18	−180.81	16.37
B3LYP/6-311+G**	156.02	−207.85	179.49	−190.82	196.03	−82.92	177.18	−160.53	16.65
				BH_4^-					
RHF/6-31G**	186.52	−27.15	186.52	−27.15	186.52	−27.15	186.52	−27.15	159.37
RHF/6-311G**	183.63	−26.87	183.63	−26.87	183.63	−26.87	183.63	−26.87	156.76
RHF/6-311+G**	185.16	−27.19	185.16	−27.19	185.16	−27.19	185.16	−27.19	157.97
B3LYP/6-31G**	189.23	−32.96	189.23	−32.96	189.23	−32.96	189.23	−32.96	156.27
B3LYP/6-311G**	185.49	−33.11	185.49	−33.11	185.49	−33.11	185.49	−33.11	152.38
B3LYP/6-311+G**	188.29	−33.20	188.29	−33.20	188.29	−33.20	188.29	−33.20	155.09

A breakdown of theoretical paramagnetic and diamagnetic magnetic shielding contributions at the boron nuclei in $[Cp^*_2B]^+$, Cp^*_2BMe, and BH_4^- are given in Table 5. In $[Cp^*_2B]^+$, magnetic dipole allowed mixing of energetically proximate occupied and virtual orbitals is undoubtedly responsible for magnetic deshielding perpendicular to the pseudo-5-fold molecular axis. Such mixing is absent perpendicular to this axis, as evidenced by the much higher shielding in this direction. It is interesting to note that both RHF and B3LYP calculations predict very small negative paramagnetic shielding contributions in $[Cp^*_2B]^+$; notably, calculations using the 6-311+G** basis set actually predict positive paramagnetic shielding contributions. There are numerous small positive paramagnetic contributions resulting from both mixing of occupied with virtual and mixing of occupied with occupied orbitals, which result in the high shielding at the boron nucleus in this molecule. Further discussion of high magnetic shielding in metallocenes can be found in a recent theoretical study of ferrocene.[49] The origin of anisotropic magnetic shielding of the boron nucleus in the trigonal planar Cp^*_2BMe molecule is analogous to that discussed by Wasylishen and co-workers for the trimesitylborane species,[11] and will not be discussed here in great detail. It should be pointed out that the magnetic shielding in Cp^*_2BMe has large negative paramagnetic shielding contributions in comparison to $[Cp^*_2B]^+$ (Table 5).

Theoretical calculations (B3LYP/6-31G**) predict the rotational barrier of the η^5-Cp* ring in $[Cp^*_2B]^+$ to be approximately 7.3 kJ mol^{-1}. The lowest energy conformer has one of the η^5-Cp* ring carbons eclipsed with the proton attached to the *ipso*-carbon of the η^1-Cp* ring. The highest energy conformation is when the η^5-Cp* ring is rotated 72° from this position. A slight decrease in Ω of −1.4 ppm with an increase in δ_{iso} of approximately 1.0 ppm is predicted as the η^5-ring is rotated into a position which is staggered compared to its original low-energy conformation. Similarly, C_Q is predicted to vary by only about 6 kHz. Owing to the ease and speed at which rings of pentahapticity are able to rotate in the absence of bulky ligands, it is very unlikely that these relatively low magnitude changes in chemical shielding and EFG will be observed even at low temperatures (<140 K).

Variable-Temperature ^{11}B MAS NMR Experiments. Lowering the temperature from 25 to −145 °C leads to very subtle changes in the ^{11}B MAS NMR spectra (Figure 6) of $[Cp^*_2B]^+$. Typically, slowing molecular motions resulting from decreasing temperature are associated with increases in C_Q. Best fit simulations of variable-temperature (VT) NMR spectra indicate that on lowering the temperature only a negligible increase (from about 1.16 to 1.17 MHz) is observed. A similarly subtle yet noticeable change in η_Q (from 0.15 to 0.24) is also seen. The isotropic chemical shift does not correlate with temperature in a linear fashion and slight changes (−41.3 → −40.4 → −40.6 → −40.8 ppm) are observed upon decreasing the temperature (25 → −30 → −90 → −145 °C). These experimental results are in qualitative agreement with theoretical predictions of a low rotational barrier, and general insensitivity of the anisotropic NMR interactions in the $[Cp^*_2B]^+$ cation to different rotational conformations.

Carbon-13 CPMAS NMR and Carbon Chemical Shielding Tensors. $^{13}C\{^1H\}$ CPMAS experiments were conducted on $[Cp^*_2B]^+$ (Figure 7), to determine carbon chemical shielding tensors. The η^5-Cp* ring is rapidly rotating, so that only one resonance is observed for each of the Cp* ring and methyl carbons, at 109.3 and 5.8 ppm, respectively. All of the carbon sites on the η^1-Cp* ring are resolved as well, with chemical shifts in close agreement with those observed in solution.[5] Room-temperature ^{13}C CPMAS experiments with variable contact times ranging from 3 to 15 ms showed little variation in cross-polarization efficiency.

A number of spinning sidebands are observed for the η^5-Cp* ring carbons as well as for the α- and β-carbons in the η^1-Cp* ring, due to chemical shielding anisotropy. These spinning sidebands can be analyzed by the Herzfeld and Berger method[23] to yield the principal components of the chemical shielding tensors of the three carbon environments mentioned above. Table 6 lists results from Herzfeld−Berger analysis along with RHF and B3LYP calculations. For the η^5-Cp* ring, results are comparable to reported ^{13}C CS tensors of Cp'_2M systems[50,51] with principal components $\delta_{11} = 157$ ppm, $\delta_{22} = 140$ ppm, $\delta_{33} = 32$ ppm, shielding anisotropy $\Omega = 124$ ppm, and a skew of $\kappa = 0.7$. Chemical shift parameters for the α- and β-carbons on the η^1-Cp* ring are similar, the main difference being a decrease in δ_{11} of about 67 ppm which increases the span of the chemical shielding tensor to $\Omega = 181$ and 186 ppm, respectively. These parameters correspond closely with previ-

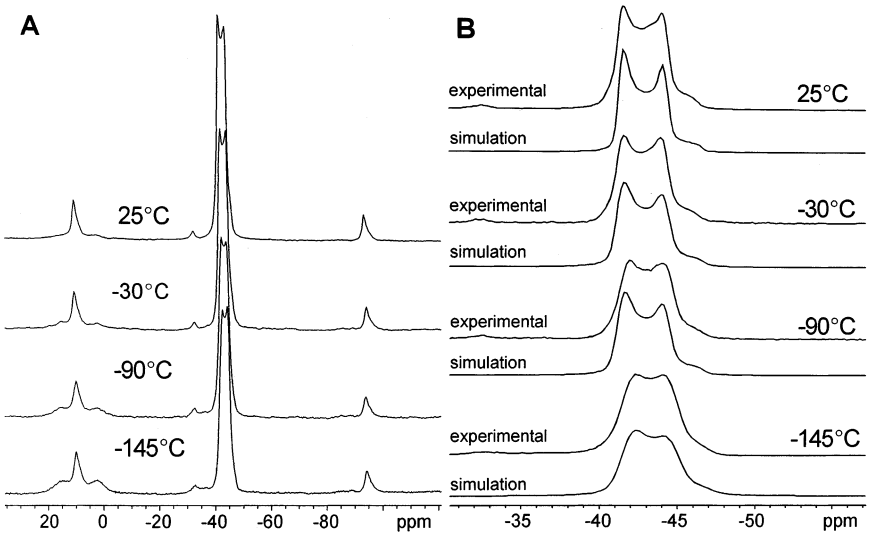

Figure 6. Variable-temperature ^{11}B MAS NMR spectra of $[Cp^*_2B]^+$ at 8.46 T. (A) Full spectral width and (B) expanded isotropic centerbands.

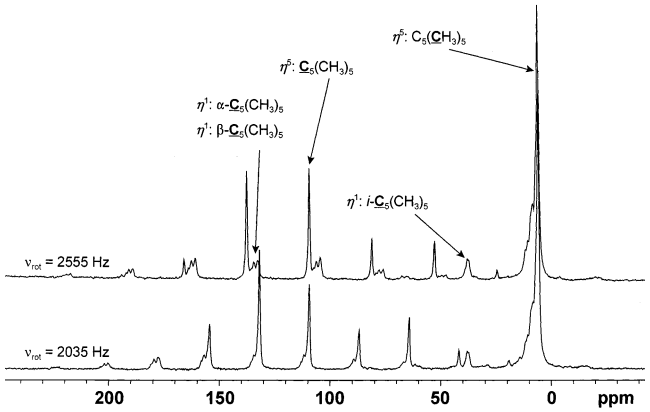

Figure 7. ^{13}C{^{1}H} CPMAS NMR spectra of $[Cp^*_2B][AlCl_4]$ at 8.46 T, υ_{rot} = 2555 and 2035 Hz.

ously measured carbon shift tensors for the η^1-rings in tetrakis-(cyclopentadienyl)titanium.[52]

A series of calculations of the ^{13}C chemical shift tensors is also presented in Table 6. For the η^5-Cp* aromatic carbons, RHF calculations tend to exaggerate the magnitude of Ω by overestimating the shielding perpendicular to the ring plane (i.e., δ_{33}). B3LYP calculations seem to predict the span more closely. Furthermore, the B3LYP calculations are also superior in predicting values of δ_{iso} and Ω for the η^1-Cp* ring. In the case of the η^5-ring, there is a discrepancy between the experimental and theoretical skews, likely resulting from averaging of the observed CS tensor due to ring motion. For the η^1-ring, skews are more accurately calculated by both methods.

Theoretically obtained ^{13}C shielding tensors for Cp* ring carbons are all oriented so the largest principal component, σ_{33}, is directed approximately perpendicular to the Cp* rings while the less shielded components, σ_{11} and σ_{22}, lie very close to the Cp* ring planes and assume a variety of different orientations (Figure 8). This is the case for all except the *ipso*-carbon on the η^1-Cp* ring, which has σ_{11} and σ_{22} positioned in such a way that the η^1-Cp* ring nearly bisects the angle between them, and σ_{33} is perpendicular to the boron−(*ipso*-carbon)−(methyl carbon) plane.

^{11}B/^{13}C/^{1}H TRAPDOR NMR of $[Cp^*_2B]^+$. In this section of the paper, we address TRAPDOR NMR effects and their relation to apparent intramolecular dynamics of $[Cp^*_2B]^+$. ^{11}B/^{13}C/^{1}H CP TRAPDOR MAS NMR spectra and control spectra (standard ^{13}C{^{1}H} CPMAS NMR spectra) of $[Cp^*_2B]^+$ acquired at 25 and −150 °C are shown in Figure 9. Not only are TRAPDOR effects visible at both temperatures, there is also considerable variation in the efficiency of cross-polarization. In the room-temperature control spectrum, cross-polarization is efficient for both the aromatic and methyl ^{13}C nuclei of the Cp* rings. Upon irradiating on the ^{11}B channel using the TRAPDOR sequence, all of the aromatic ^{13}C signals disappear almost completely, while the ^{13}C methyl signals remain relatively unchanged. This is indicative of relatively strong dipolar coupling between the ^{11}B and aromatic ^{13}C nuclei in both Cp* rings, even in light of rapid rotation of the η^5-Cp* ring and the large internuclear distances between boron and ortho and meta carbons in the η^1-Cp* ring. Dipolar coupling constants may be easily calculated from the crystal structure of the $[Cp^*_2B]^+$ cation, and scale as the inverse cube of the internuclear distance. Dipolar coupling constants between the η^5-Cp* ring carbons and boron are quite large, with $R_{DD}(^{11}B,^{13}C)$ = 1760 Hz, and $R_{DD}(^{11}B,^{13}C)$ = 2430 Hz between boron and the directly bound "ipso" carbon of the η^1-Cp* ring. ^{11}B, ^{13}C dipolar coupling constants range from 250 to 650 Hz for the remainder of the ^{13}C nuclei in the molecule. At −150 °C, with various spinning speeds and contact times, CP to the η^5-Cp* aromatic and methyl carbons drops substantially (though peaks can still be distinguished), and the η^1-Cp* carbon sites can be seen clearly. Notably, much definition can be seen in the methyl group region (see inset, Figure 9). The only clearly discernible difference in the CP TRAPDOR spectrum at −150 °C is at the "ipso" carbon (δ 37.0 ppm, marked with an asterisk), indicating that this is the only carbon nucleus still strongly dipolar coupled to boron. Closer examination reveals that there is a 25−40% decrease in signal intensity for the η^5-Cp* aromatic carbons, much less than observed at room temperature (though this is difficult to strictly quantify due to the reduction in CP efficiency). Signal intensity decrease is not observed for the remainder of the carbon sites in the −150 °C TRAPDOR spectra.

This set of results initially seems to be counterintuitive, as stronger dipolar couplings between ^{11}B and ^{13}C are expected at lower temperatures as the η^5-Cp* ring motion slows down, perhaps leading to a stronger TRAPDOR effect. In addition, variable contact time CPMAS experiments at various spinning speeds fail to improve the CP efficiency to the η^5-carbons at low temperatures. However, the TRAPDOR results do suggest

TABLE 6: Experimental and Theoretical Carbon-13 Chemical Shift Tensors[a] in $[Cp^*_2B]^+$

site	δ_{11} (ppm)	δ_{22} (ppm)	δ_{33} (ppm)	δ_{iso}[b] (ppm)	Ω[b] (ppm)	κ[b]
			Experimental			
η^5: $C_5(CH_3)_5$				5.9		
η^5: $C_5(CH_3)_5$	156	140	32	109.3	124	0.73
η^1: *i*-$C_5(CH_3)_5$				37.7		
η^1: α-$C_5(CH_3)_5$	224	135	43	134.2	181	0
η^1: β-$C_5(CH_3)_5$	224	144	38	135.5	186	0.14
			RHF/6-31G**			
η^5: $C_5(CH_3)_5$	151.0	139.7	19.3	103.3	131.7	0.83
	149.4	147.6	15.9	104.3	133.5	0.97
	149.2	145.4	15.1	103.2	134.1	0.94
	147.7	144.6	15.2	102.5	132.5	0.95
	148.8	145.1	17.3	103.7	131.5	0.94
η^1: *i*-$C_5(CH_3)_5$	41.7	35.6	10.3	29.2	31.4	0.61
η^1: α-$C_5(CH_3)_5$	238.8	129.6	28.7	132.4	210.2	−0.04
	236.7	127.8	29.1	131.2	207.6	−0.05
η^1: β-$C_5(CH_3)_5$	244.2	120.2	39.8	134.7	204.4	−0.21
	240.9	121.3	39.6	133.9	201.3	−0.19
			RHF/6-311G**			
η^5: $C_5(CH_3)_5$	148.0	134.4	9.2	97.2	138.8	0.80
	146.6	143.1	5.5	98.4	141.1	0.95
	146.3	140.9	5.0	97.4	141.3	0.92
	144.7	140.1	5.1	96.7	139.6	0.93
	145.3	140.4	7.1	97.6	138.2	0.93
η^1: *i*-$C_5(CH_3)_5$	33.3	26.4	−0.9	19.6	34.2	0.59
η^1: α-$C_5(CH_3)_5$	245.8	125.0	20.0	130.3	225.7	−0.07
	243.6	123.2	20.5	129.1	223.2	−0.08
η^1: β-$C_5(CH_3)_5$	249.3	113.0	30.5	130.9	218.8	−0.25
	245.5	114.1	30.4	130.0	215.2	−0.22
			RHF/6-311+G**			
η^5: $C_5(CH_3)_5$	148.3	134.9	9.5	97.6	138.8	0.81
	147.2	143.7	5.8	98.9	141.4	0.95
	146.9	141.4	5.3	97.8	141.6	0.92
	145.4	140.5	5.4	97.1	140.0	0.93
	145.8	141.0	7.3	98.0	138.5	0.93
η^1: *i*-$C_5(CH_3)_5$	33.5	27.0	−0.6	20.0	34.1	0.62
η^1: α-$C_5(CH_3)_5$	246.3	126.0	20.3	130.9	226.0	−0.06
	244.2	124.3	20.7	129.7	223.5	−0.07
η^1: β-$C_5(CH_3)_5$	249.6	113.7	30.8	131.4	218.7	−0.24
	245.8	114.8	30.7	130.4	215.1	−0.22
			B3LYP/6-31G**			
η^5: $C_5(CH_3)_5$	158.0	152.1	39.1	116.4	118.9	0.90
	160.5	156.7	35.5	117.6	125.0	0.94
	158.5	154.4	34.6	115.8	123.9	0.93
	157.7	153.8	34.9	115.4	122.9	0.94
	157.7	155.6	37.1	116.8	120.6	0.96
η^1: *i*-$C_5(CH_3)_5$	61.0	55.2	30.8	49.0	30.2	0.62
η^1: α-$C_5(CH_3)_5$	224.3	148.5	47.5	140.1	176.8	0.14
	223.2	146.2	48.0	139.1	175.3	0.12
η^1: β-$C_5(CH_3)_5$	231.6	141.3	57.4	143.4	174.2	−0.04
	228.6	142.2	57.1	142.6	171.4	−0.01
			B3LYP/6-311G**			
η^5: $C_5(CH_3)_5$	156.2	146.9	25.0	109.3	131.2	0.86
	156.3	154.5	21.7	110.8	134.6	0.97
	154.1	151.8	21.1	109.0	133.0	0.97
	153.3	151.5	21.4	108.7	131.8	0.97
	153.1	152.7	23.0	109.6	130.2	0.99
η^1: *i*-$C_5(CH_3)_5$	51.2	44.8	16.1	37.4	35.1	0.64
η^1: α-$C_5(CH_3)_5$	232.3	143.2	36.1	137.2	196.2	0.09
	231.1	140.9	36.5	136.1	194.6	0.07
η^1: β-$C_5(CH_3)_5$	238.1	135.1	44.8	139.3	193.3	−0.07
	234.4	136.2	44.7	138.4	189.7	−0.03
			B3LYP/6-311+G**			
η^5: $C_5(CH_3)_5$	157.5	149.8	25.6	111.0	132.0	0.88
	158.0	156.7	23.8	112.8	134.2	0.98
	156.5	153.2	22.6	110.8	133.8	0.95
	155.2	153.6	22.8	110.5	132.4	0.98
	155.6	154.2	23.9	111.2	131.7	0.98
η^1: *i*-$C_5(CH_3)_5$	52.5	44.6	16.4	37.8	36.1	0.57
η^1: α-$C_5(CH_3)_5$	234.4	147.1	36.2	139.2	198.2	0.12
	233.1	144.3	36.5	137.9	196.5	0.10
η^1: β-$C_5(CH_3)_5$	240.6	136.7	45.5	140.9	195.0	−0.07
	236.3	137.7	45.9	140.0	190.5	−0.04

[a] Absolute chemical shieldings are converted to chemical shifts with the formula $\sigma_{ref} - \sigma_{sample}$, where σ_{ref} is the absolute chemical shielding of C≡O. See Experimental Section for details. [b] $\delta_{iso} = (\delta_{11} + \delta_{22} + \delta_{33})/3$, $\Omega = \delta_{11} - \delta_{33}$, and $\kappa = 3(\delta_{22} - \delta_{iso})/\Omega$.

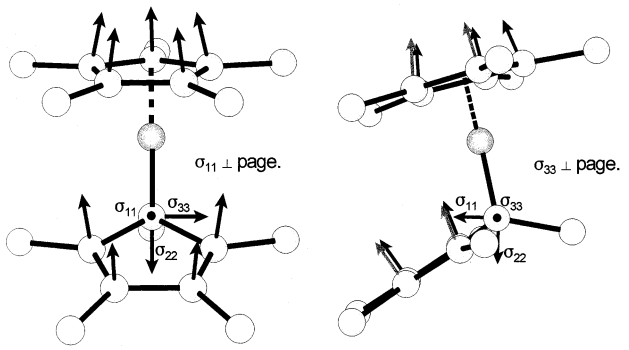

Figure 8. Orientation of theoretical carbon chemical shielding tensors of aromatic carbons in $[Cp^*_2B]^+$. Arrows signify direction of σ_{33} at all carbons with σ_{11} and σ_{22} components omitted for clarity. The full chemical shielding tensor orientation is shown for the ipso carbon in the η^1-Cp* ring.

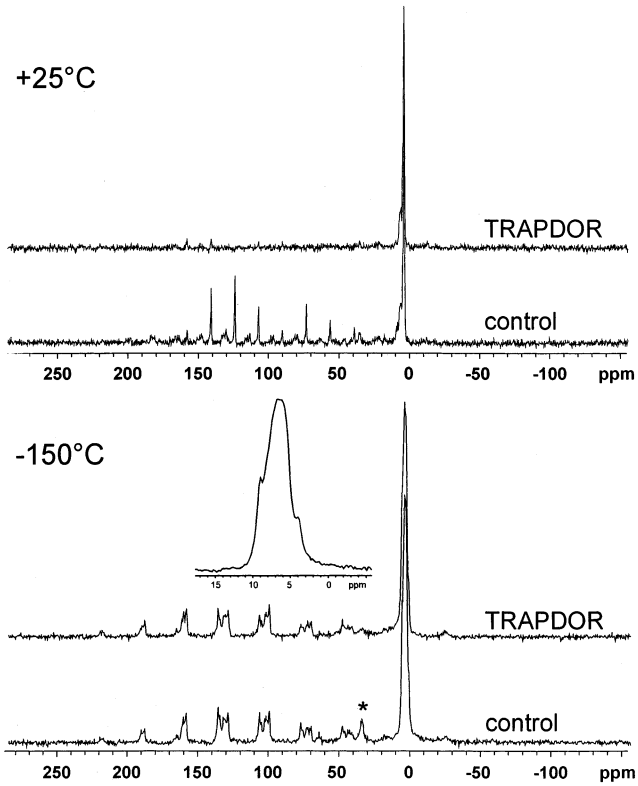

Figure 9. $^{11}B/^{13}C/^1H$ CPMAS TRAPDOR and control CPMAS NMR spectra of $[Cp^*_2B][AlCl_4]$ at +25 and −150 °C. Inset of spectrum acquired at −150 °C shows detail of individual methyl carbon sites on the η^1-Cp* ring.

that a sigmatropic exchange mechanism is occurring for the η^1-Cp* ring. The exchange process involves "jumplike" rotation of the η^1-Cp* ring such that each of the aromatic η^1-Cp* carbons spends a finite amount of time (shorter than the time scale of the TRAPDOR experiment) proximate to the boron nucleus. As a consequence, a very large TRAPDOR effect is experienced by all of the aromatic η^1-Cp* carbon nuclei, since ^{11}B and ^{13}C will be dipolar coupled for a finite amount of time. At lower temperatures, the exchange rate is slower than the time scale of the TRAPDOR experiment (irradiation occurs over a single 100 μs rotor period), and thus only the directly bound "ipso" aromatic carbon nucleus experiences the TRAPDOR effect, while no intensity loss is observed for the remainder of the carbon sites in the η^1-Cp* ring. This preliminary interpretation of NMR data and chemical exchange is consistent with the concept of a reorienting η^1-Cp* ring (perhaps passing through an η^2-Cp* transition state).[9] Such sigmatropic rearrangements have been previously studied by ^1H wide-line and $^{13}C/^1H$ CPMAS NMR experiments in a number of monohapto-Cp containing transition metal metallocenes such as Cp_4Ti,[52] CpHgX (X = Cl, Br, I), and $Cp_2Fe(CO)_2$.[53] Double- and triple-resonance NMR experiments of this nature seem very promising for examining such intramolecular motions; currently, additional one- and two-dimensional experiments at variable temperatures are being conducted in our laboratory to probe ring motion and effects of intramolecular dynamics on cross-polarization and cross-relaxation in this complex and analogous substances.

Conclusions

The central transitions of solid-state ^{11}B MAS and static NMR spectra are markedly affected by anisotropic quadrupolar and chemical shielding interactions, which in turn are strongly influenced by the local symmetry and structure of the bis-(pentamethylcyclopentadienyl)boron cation. Comparable data have been obtained for bis(pentamethylcyclopentadienyl)-methylborane. Two structurally different metallocenes exhibit vastly different quadrupolar coupling constants and chemical shielding tensor spans and symmetries, suggesting that chemically similar metallocenes may also be differentiated by simple solid-state NMR methods (albeit with less noticeable changes in the anisotropic NMR parameters). Ab initio calculations of both chemical shielding and EFG tensors are in very good agreement with experimentally determined parameters, demonstrating the useful prognosticative nature of these calculations. Double- and triple-resonance $^{13}C/^{11}B/^1H$ NMR experiments performed at variable temperatures support previously observed sigmatropic rearrangements of η^1-Cp′ rings and show promise for further examinations of ring motion in metallocene complexes. However, for metallocenes with low internal rotation barriers, it may be necessary to drop to very low temperatures (e.g., $<50-60$ K) to observe any significant effects on solid-state NMR spectra of the central metal nucleus. We believe that acquiring and analyzing NMR spectra of metal quadrupolar nuclei in metallocenes, in combination with theoretical computation of anisotropic NMR interaction tensors, provides an excellent means of probing metallocene structure, dynamics, and chemistry. We hope that our work will encourage further work of this nature on this important class of organometallic compounds.

Acknowledgment. We thank Professor Clare P. Grey and Mr. Peter Chupas of the State University of New York at Stony Brook for solid-state NMR time on the Chemagnetics 360 MHz wide-bore spectrometer, as well as for help with setting up experiments and acquiring spectra. We thank Dr. Andreas Voigt for initial preparation and crystallography of several group 13 metallocenes. We also thank Professor Doug Stephan (University of Windsor) for use of his gloveboxes for sample preparation. R.W.S. is grateful to Imperial Oil for an Imperial Oil Research Grant, and the National Science and Engineering Research Council (NSERC) of Canada for funds in the form of an Operation Grant and Collaborative Research and Development Grant. R.W.S. also thanks the Canadian Foundation for Innovation and the Ontario Innovation Trust for funding of the new solid-state NMR facility at the University of Windsor. A.H.C. thanks the National Science Foundation (NSF) and the Robert A. Welch Foundation for financial support.

Supporting Information Available: Tables of X-ray crystallographic data and Cartesian coordinates used for ab initio

calculations. This material is available free of charge via the Internet at http://pubs.acs.org.

References and Notes

(1) *Metallocenes Vol. 1: Synthesis, Reactivity, Applications*; Togni, A., Halterman, R. L., Eds.; Wiley-VCH Verlag GmbH: Weinheim, 1998.

(2) Harder, S. *Coord. Chem. Rev.* **1998**, *176*, 17.

(3) Jutzi, P.; Burford, N. *Chem. Rev.* **1999**, *99*, 969.

(4) Beswick, M. A.; Palmer, J. S.; Wright, D. S. *Chem. Soc. Rev.* **1998**, *27*, 225.

(5) Voigt, A.; Fillipponi, S.; Macdonald, C. L. B.; Gorden, J. D.; Cowley, A. H. *Chem. Commun.* **2000**, 911.

(6) Jutzi, P.; Seufert, A. *J. Organomet. Chem.* **1978**, *161*, 5.

(7) Margl, P.; Schwartz, K.; Blöchl, P. E. *J. Am. Chem. Soc.* **1994**, *116*, 11177.

(8) del Mar Conejo, M.; Fernandez, R.; Gutierrez-Puebla, E.; Monge, A.; Ruiz, C.; Carmona, E. *Angew. Chem., Int. Ed.* **2000**, *39*, 1949. See also: del Mar Conejo, M.; Fernandez, R.; Carmona, E.; Gutierrez-Puebla, E.; Monge, A. *Organometallics* **2001**, *20*, 2434.

(9) Kwon, O.; McKee, M. L. *J. Phys. Chem. A* **2001**, *105*, 10133.

(10) Pyykkö, P. *Z. Naturforsch. A* **1992**, *47*, 189.

(11) Bryce, D. L.; Wasylishen, R. E.; Gee, M. *J. Phys. Chem. A* **2001**, *105*, 3633.

(12) Kroeker, S.; Stebbins, J. F. *Inorg. Chem.* **2001**, *40*, 6239.

(13) *Multinuclear NMR*; Mason, J., Ed.; Plenum Press: New York, 1987.

(14) (a) Grey, C. P.; Veeman, W. S. *Chem. Phys. Lett.* **1992**, *192*, 379. (b) Grey, C. P.; Veeman, W. S.; Vega, A. J. *J. Chem. Phys.* **1993**, *98*, 7711.

(15) Otwinowski, Z.; Minor, W. DENZO-SMN. *Macromolecular Crystallography*; Carter, C. W., Jr., Sweets, R. M., Eds.; Methods in Enzymology 276; Academic Press: New York, 1997; Part A, pp 307−326.

(16) Altomare, A.; Burla, M. C.; Camalli, M.; Cascarano, G., Giacovazzo, C.; Guagliardi, A.; Moliterni, A. G. G.; Polidori, G.; Spagna, R. *SIR97, A program for crystal structure solution*; 1997.

(17) Sheldrick, G. M. *SHELXL93, Program for the Refinement of Crystal Structures*; University of Gottingen: Gottingen, Germany, 1994.

(18) *International Tables for X-ray Crystallography*; Wilson, A. J. C., Ed.; Kluwer Academic Press: Boston, 1992; Vol. C, Tables 4.2.6.8 and 6.1.1.4.

(19) Sheldrick, G. M. *SHELXTL/PC*, Version 5.03; Siemens Analytical X-ray Instruments, Inc.: Madison, WI, 1994.

(20) Hayashi, S.; Hayamizu, K. *Bull. Chem. Soc. Jpn.* **1989**, *62*, 2429.

(21) WSOLIDS (Version 1.17.28) software for simulations of solid-state NMR powder patterns, developed by Dr. Klaus Eichele in Prof. Roderick Wasylishen's laboratory, Dalhousie University.

(22) Alderman, D. W.; Solum, M. S.; Grant, D. M. *J. Chem. Phys.* **1986**, *84*, 3717.

(23) (a) Herzfeld, J.; Berger, A. E. *J. Chem. Phys.* **1980**, *73*, 6021. (b) Maricq, M. M.; Waugh, J. S. *J. Chem. Phys.* **1979**, *70*, 3300.

(24) Bak, M.; Rasmussen, J. T.; Nielsen, N. C. *J. Magn. Reson.* **2000**, *147*, 296.

(25) Frisch, M. J.; Trucks, G. W.; Schlegel, H. B.; Scuseria, G. E.; Robb, M. A.; Cheeseman, J. R.; Zakrzewski, V. G.; Montgomery, J. A., Jr.; Stratmann, R. E.; Burant, J. C.; Dapprich, S.; Millam, J. M.; Daniels, A. D.; Kudin, K. N.; Strain, M. C.; Farkas, O.; Tomasi, J.; Barone, V.; Cossi, M.; Cammi, R.; Mennucci, B.; Pomelli, C.; Adamo, C.; Clifford, S.; Ochterski, J.; Petersson, G. A.; Ayala, P. Y.; Cui, Q.; Morokuma, K.; Malick, D. K.; Rabuck, A. D.; Raghavachari, K.; Foresman, J. B.; Cioslowski, J.; Ortiz, J. V.; Baboul, A. G.; Stefanov, B. B.; Liu, G.; Liashenko, A.; Piskorz, P.; Komaromi, I.; Gomperts, R.; Martin, R. L.; Fox, D. J.; Keith, T.; Al-Laham, M. A.; Peng, C. Y.; Nanayakkara, A.; Challacombe, M.; Gill, P. M. W.; Johnson, B.; Chen, W.; Wong, M. W.; Andres, J. L.; Gonzalez, C.; Head-Gordon, M.; Replogle, E. S.; Pople, J. A. *Gaussian 98*, revision A.9; Gaussian, Inc.: Pittsburgh, PA, 1998.

(26) (a) Becke, A. D. *J. Chem. Phys.* **1993**, *98*, 5648. (b) Becke, A. D. *Phys. Rev. A* **1988**, *38*, 3098.

(27) Lee, C.; Yang, W.; Parr, R. G. *Phys. Rev. B* **1988**, *37*, 785.

(28) (a) Ditchfield, R. *Mol. Phys.* **1974**, *27*, 789. (b) Wolinski, K.; Hinton, J. F.; Pulay, P. *J. Am. Chem. Soc.* **1990**, *112*, 8251 and references therein.

(29) Jameson, A. K.; Jameson, C. J. *Chem. Phys. Lett.* **1987**, *134*, 461.

(30) Mehring, M. *Principles of High-Resolution NMR in Solids*, 2nd ed.; Springer-Verlag: New York, 1983.

(31) Haeberlen, U. *High-Resolution NMR in Solids;* Academic Press: New York, 1976.

(32) Mason, J. *Solid State Nucl. Magn. Reson.* **1993**, *2*, 285.

(33) Power, W. P.; Wasylishen, R. E.; Mooibroek, S.; Pettitt, B. A.; Danchura, W. *J. Phys. Chem.* **1990**, *94*, 591.

(34) Eichele, K.; Wasylishen, R. E.; Nelson, J. H. *J. Phys. Chem. A* **1997**, *101*, 5463.

(35) Zare, R. N. *Angular Momentum—Understanding Spatial Aspects in Chemistry and Physics*; John Wiley & Sons: New York, 1988.

(36) (a) Knop, O.; Palmer, E. M.; Robinson, R. W. *Acta Crystallogr., Sect. A* **1975**, *31*, 19. (b) Knop, O. *Acta Crystallogr., Sect. A* **1976**, *32*, 147.

(37) Akitt, J. W.; McDonald, W. S. *J. Magn. Reson.* **1984**, *58*, 401.

(38) Benn, R.; Lehmkuhl, H.; Mehler, K.; Rufińska, A. *Angew. Chem., Int. Ed. Engl.* **1984**, *23*, 534.

(39) Dohmeier, C.; Schnöckel, H.; Robl, C.; Schneider, U.; Ahlrichs, R. *Angew. Chem., Int. Ed. Engl.* **1993**, *32*, 1655.

(40) Janiak, C.; Schumann, H.; Stader, C.; Wrackmeyer, B.; Zuckerman, J. J. *Chem. Ber.* **1988**, *121*, 1745.

(41) (a) Helgaker, T.; Jaszuński, M.; Ruud, K. *Chem. Rev.* **1999**, *99*, 293. (b) Buhl, M.; Kaupp, M.; Malkina, O. L.; Malkin, V. G. *J. Comput. Chem.* **1999**, *20*, 91. (c) de Dios, A. C. *Prog. Nucl. Magn. Reson. Spectrosc.* **1996**, *29*, 229. (d) Jameson, C. J. *Annu. Rev. Phys. Chem.* **1996**, *47*, 135. (e) *Nuclear Magnetic Shielding and Structure*; Tossell, J. A., Ed.; NATO ASI Series 386; Kluwer Academic Publishers: Dordrecht: The Netherlands, 1993.

(42) (a) Fukui, H. *Prog. Nucl. Magn. Reson. Spectrosc.* **1999**, *35*, 267. (b) Contreras, R. H.; Peralta, J. E.; Giribet, C. G.; De Azua, M. C.; Facelli, J. C. *Annu. Rep. NMR Spectrosc.* **2000**, *41*, 55.

(43) (a) Marian, C. M.; Gastreich, M. *Solid State Nucl. Magn. Reson.* **2001**, *19*, 29. (b) Mauri, F.; Vast, N.; Pickard, C. J. *Phys. Rev. Lett.* **2001**, *87*, 5506.

(44) (a) Blaha, P.; Schwarz, K.; Herzig, P. *Phys. Rev. Lett.* **1985**, *54*, 1192. (b) Blaha, P.; Schwarz, K.; Faber, W.; Luitz, J. *Hyperfine Interact.* **2000**, *126*, 389.

(45) Lucken, E. A. C. *Nuclear Quadrupole Coupling Constants*; Academic Press: New York, 1969.

(46) (a) Mitchell, D. W. *Phys. Rev. B* **1996**, *53*, 7684. (b) Hemmingsen, L.; Ryde, U. *J. Phys. Chem.* **1996**, *100*, 4803. (c) Bryant, P. L.; Harwell, C. R.; Wu, K.; Fronczek, F. R.; Hall, R. W.; Butler, L. G. *J. Phys. Chem. A* **1999**, *103*, 5246.

(47) Schwarz, K.; Ambrosch-Draxl, C.; Blaha. P. *Phys. Rev. B* **1990**, *42*, 2051.

(48) Bailey, W. C. *J. Mol. Spectrosc.* **1997**, *185*, 403.

(49) Schreckenbach, G. *J. Chem. Phys.* **1999**, *110*, 11936.

(50) Orendt, A. M.; Facelli, J. C.; Jiang, Y. J.; Grant, D. M. *J. Phys. Chem. A* **1998**, *102*, 7692.

(51) (a) Wemmer, D. E.; Ruben, D. J.; Pines, A. *J. Am. Chem. Soc.* **1981**, *103*, 28. (b) Wemmer, D. E.; Pines, A. *J. Am. Chem. Soc.* **1981**, *103*, 34.

(52) Heyes, S. J.; Dobson, C. M. *J. Am. Chem. Soc.* **1991**, *113*, 463.

(53) Campbell, A. J.; Fyfe, C. A.; Goel, R. G.; Maslowsky, E.; Senoff, C. V. *J. Am. Chem. Soc.* **1972**, *94*, 8387.